LETTER

Wafer-scale fabrication of high-density nanoslit arrays for surface-enhanced Raman spectroscopy

IOP Publishing
Letters
Nanotechnology
Nanotechnology 27 (2016) 49LT01 (8pp)
doi:10.1088/0957-4484/27/49/49LT01

Letter

Wafer-scale fabrication of high-density nanoslit arrays for surface-enhanced Raman spectroscopy

Mingliang Jin[1,2], Yunfei Zhu[1,2], Albert van den Berg[2,3], Zhang Zhang[1,2], Guofu Zhou[1,2] and Lingling Shui[1,2]

[1] Institute of Electronic Paper Displays, South China Academy of Advanced Optoelectronics, South China Normal University, Guangzhou 510006, People's Republic of China
[2] Joint International Research Laboratory of Optical Information of the Chinese Ministry of Education, South China Normal University, Guangzhou 510006, People's Republic of China
[3] BIOS/Lab-on-a-Chip Group, MESA+ Institute for Nanotechnology, University of Twente, Drienerlolaan 5, 7522 NB Enschede, The Netherlands

E-mail: shuill@m.scnu.edu.cn

Received 23 August 2016, revised 13 October 2016
Accepted for publication 14 October 2016
Published 10 November 2016

Abstract

Surfaces with a periodic nanostructure and controllable feature size are sought after for optical applications, and the fabrication of such surfaces in large areas with high reproducibility, good stability and low deviation is very important. We present a strategy to fabricate large-area nanoslit arrays with controllable pitches and gaps. Au nanoslit arrays with gaps down to around 10 nm and a high gap density of $2.0 \times 10^4\ cm^{-1}$ have been fabricated, which can greatly enhance the near-field electromagnetic field to achieve localized surface plasmon resonance (LSPR). An averaged surface-enhanced Raman scattering analytical enhancement factor of 8.0×10^7 has been achieved on the substrate using a 633 nm laser source and the 'coupling effect' of LSPR of the nanoslits.

Keywords: nanoslits, nanogaps, wafer-scale fabrication, localized surface plasmon resonance, surface enhanced Raman scattering

(Some figures may appear in colour only in the online journal)

1. Introduction

Localized surface plasmon resonance (LSPR) on noble metal (Au, Ag or Cu) surfaces has attracted significant attention due to its ability to enhance the near-field electromagnetic field on a nanostructure surface. A noble metal nanogap can further enhance the electromagnetic field when the gap distance is less than 10 nm by to the 'coupling effect' phenomenon [1]. The enhanced electromagnetic field on the surface of nanogaps can dramatically enhance the Raman scattering of the molecules localized in the nanogaps. Specific regions like the nanogaps on a substrate are therefore called Raman 'hot-spots'. A surface-enhanced Raman scattering (SERS) substrate typically consists of millions of Raman 'hot-spots'. Since Raman spectra act as a fingerprint for information on vibration of molecules, SERS has been widely applied in biology, chemistry, physics and materials science for label-free sensing and detection [2].

Up to now, various SERS substrates have been designed, fabricated and investigated [3]. Nanogap substrates have proved to be one of the most promising structures for generating LSPR and SERS. In the past decades, different approaches have been reported for fabricating nanogap substrates [4]. Nanoparticle aggregations were developed in the 1990s as the earliest nanogap system. This nanoparticle system was easy to prepare and could strongly enhance the

Raman signal even for single-molecule Raman detection [5]. However, the gap distance between two nanoparticles is difficult to control and the sample-to-sample reproducibility of the Raman signal is relatively poor. Size-controllable nanogaps have commonly been fabricated using top-down nanofabrication techniques like electron beam lithography [6], electron migration [7], focused ion beam lithography [8], laser interference lithography [9] and so on [10]. However, these techniques are expensive and time-consuming. It generally takes a relatively long time to fabricate a SERS substrate with a reasonable working area (e.g. 1 cm^2). A substrate with densely packed 'hot-spots' could also be quickly fabricated via film deposition and annealing treatment; however, this technique is dependent of equipment and environment [11, 12]. Large-area high-resolution nano-patterning techniques such as deep-ultraviolet stepper photolithography are standard for semiconductor manufacturing; however, these techniques are expensive and accessible only to large integrated circuit manufacturers.

Recently, a few large-area nanogap substrates have been fabricated using photolithography combined with metal layer deposition technology [13]. These vertical nanogaps were mainly controlled by the thickness of the metal layer which was precisely controlled by atomic layer deposition (ALD). A periodical nano-dome array has been fabricated using a low-cost nano-replica moulding technique [14]. However, the gap distance is dozens of nanometres. Nanogaps fabricated by nano-imprinting combined with nano-coating and etching have also been reported [15]. By controlling the thickness of the spacer polymer, nanogaps of tens of nanometres have been achieved. Nowadays, researchers are focusing on fabricating nanogaps with a large area and precisely controllable nanogap distance.

Laser interference lithography (LIL) is a simple and fast patterning technology [9]. It has been widely applied in manufacturing for fabricating nano-grading substrates [16], nano-pyramids [17], 3D nanostructures [18] and nano-dots [19]. With a tuneable reflection angle, an altered pattern periodicity can be achieved. LIL is regarded as an ideal tool to quickly pattern large-area substrates with high resolution and relatively low cost. The efficiency of LIL is much higher than that of electron beam lithography, as it can pattern the whole surface of a standard silicon wafer (e.g. a 4 inch/100 mm diameter wafer), with about 100 nm resolution in one step within 1 min. However, the fabrication resolution of LIL is highly dependent on the wavelength of the light source, and it is difficult to achieve a resolution of less than 50 nm in most cases. Edge lithography is defined as a technique in which the edge of the original pattern becomes a feature of the ultimate pattern. Edge lithography has mainly been applied for the nanofabrication of sub-20 nm structures [20]. It is a simple technique with a long history. Its main advantage is that the edge modification can be applied as the etching mask, for which the local modification can be described as a localized nanofabrication technique.

In this work we present a new strategy aiming to fabricate small-size nanogaps (nanoslits) with at a high density on large-area (standard wafer-scale size) surfaces by combining the three techniques of LIL, edge lithography and thin film deposition. LIL was implemented to pattern regular nanoslit arrays of fine features on the large-area substrate without complex optical systems or photomasks. Edge lithography and anisotropic wet-etching were then applied to fabricate a second level nanostructure on the previously patterned substrate to overcome the drawback of LIL (namely its relatively low fabrication resolution). The edge to edge distance of the nanoslits could later be precisely adjusted by changing the thickness of the deposited gold layer. The large-area and size-controllable metal nanoslits (nanogaps) fabricated using this 'top-down' fabrication strategy show extremely high LSPR since the nanoslits could be precisely tuned to match the wavelength of the excitation source to provide optimal local electromagnetic field enhancement. This is an open nanogap system for detection, which provides a convenient and efficient platform for the interaction of the adsorbed probe molecules with the strong plasmonic near-field in the nanoslits, as previously reported [11, 12].

2. Methods

2.1. Materials

4-Methylbenzenethiol (4-MBT, 98%) and methanol (99.9%) was purchased from Sigma-Aldrich, China. Polymethyl methacrylate (PMMA) was purchased from MicroChem Corp., USA. Methyl isobutyl, ketone, isopropanol, hydrofluoric acid (HF), potassium hydroxide (KOH) and phosphoric acid (H_3PO_4) were purchased from Merck Millipore, Germany. Deionized (DI) water (18.2 MΩ at 25 °C) was prepared using a Milli-Q Plus water purification system (Sichuan Wortel Water Treatment Equipment Co. Ltd, Sichuan, China). All chemicals were used as-received.

2.2. Instrumentation

2.2.1. Reflectance measurements. Normal reflection measurements were performed with a white light source (100 W tungsten xenon lamp) focused on the Au nanoslit surface with a 20× microscope objective (NA = 0.29, Mitutoyo, M Plan APO). The reflected light was collected through the same objective and detected by a spectrometer (USB2000+, Ocean Optics) through an optical fibre (QP450-1-XSR, Ocean Optics). All the measurements were calibrated with a flat (non-patterned) silicon wafer with a deposited Au film using the same nominal metal thickness on the nanoslit surface. The thickness of the Au layer was measured with a stylus profiler (Dektak XT, Bruker, Germany) on the flat silicon wafer.

2.2.2. Raman measurements. 4-MBT (98%, Sigma-Aldrich) was used to characterize SERS effects. The nanoslit array substrate was completely immersed in 10 ml of 4 mM methanol solution for 30 min, then rinsed with methanol three times and blow dried with pure nitrogen gas. The dried nanoslit substrate was placed on the stage of the

Raman instrument for measurements. The Raman spectra of 4-MBT molecules were measured using a micro-Raman system (Renishaw inVia Raman Microscope) based on a Leica microscope. A 633 nm He–Ne laser (Renishaw, RL633 laser) was employed as the excitation source. The laser beam was focused on the sample through a 50× objective (NA = 0.5, Olympus). The diameter of the laser spot was 1.54 μm. The elastically scattered laser excitation was removed with an edge filter. The integration time for all Raman spectra was 10 s.

2.2.3. Scanning electron microscopy (SEM) and atomic force microscopy (AFM) imaging. SEM images of the Au nanoslits samples were measured using an Ultra 55 or LEO 1550 (Zeiss, Germany). The nanogap distance was calculated by converting the measured SEM image to a binary image and counting the number of pixels crossing the line. AFM images were obtained using Cypher™ (Asylum Research, USA) in tapping mode.

3. Results and discussion

Standard 4 inch (100 mm diameter) silicon wafers with thickness of 525 μm were used for all sample fabrication procedures. A scheme of the fabrication process is shown in figure 1. Firstly, 50 nm low-stress silicon nitride (SiN) was deposited on the wafer by low-pressure chemical vapour deposition (pressure 100 mTorr, H_2SiCl_2 77.5 sccm, NH_3 20 sccm, temperature 850 °C, deposition rate 4 nm min^{-1}, refractive index 2.2). On top of the SiN, a layer of 100 nm PMMA (MicroChem Corp., USA) was spin-coated, exposed with LIL and then developed to form a reactive ion etching (RIE) mask transferring the gap pattern to the SiN layer. The LIL exposure along the length of the SiN templates was aligned to the [110] direction of the (100) silicon wafers using the flat wafer as the reference. The exposed regions were developed in a methyl isobutyl and ketone isopropanol solution with a volume ratio of 1:3 for 30 s, then immersed in isopropyl alcohol to stop the development process. The patterned PMMA is shown in figure 1(a). The LIL pattern here determines the pitch of the nanoslit array.

The exposed SiN regions were then removed using RIE (parallel plate reactor; pressure 10 mTorr, RF 13.56 MHz, power 60 W, electrode voltage 500 V, electrode temperature 10 °C, CHF_3 25 sccm, O_2 5 sccm, etch rate 60 nm min^{-1}) followed by removal of the remaining PMMA and surface cleaning with oxygen plasma. Prior to silicon etching, the native oxide on the exposed silicon regions was removed by immersing in 1 wt% HF solution for 1 min and subsequent rinsing with deionized water. The silicon was etched in a 1 wt% KOH solution at 55 °C with stirring for 45 s and rinsed with deionized water for 2 min. Different crystal planes were etched anisotropically by the hydroxide ions in the alkaline solution; (111) planes have the lowest etching rate and (100) and (110) planes have higher etching rates. This etching process resulted in a well-controlled 'V'-shaped groove profile in the silicon layer, as shown in figure 1(b). The pitch and depth of the 'V'-shaped grooves could be controlled by LIL and the wet-etching time. Through an oxidation process, the unprotected area changed to silicon oxide (figure 1(c)), which also served as the hard mask after removing the SiN on the ridge of the grooves with 85 wt% H_3PO_4 solution at 180 °C (figure 1(d)). After the SiN layer had been removed, the same KOH anisotropic wet-etching process was used to create nanoslits on the top of the ridges (figure 1(e)). A gold layer was then deposited by a metal sputtering system (KYKY, SBC-12 ion sputtering equipment). The thickness of the metal film was controlled by the sputtering current and time. Au layer deposition formed the final metal nanoslits, as shown in figure 1(f). The gap distance between the nanoslits could therefore be precisely controlled by the metal deposition process. Figure 1(g) shows an overall cross-sectional view of the obtained nanoslit array.

A standard 4-inch Si-wafer substrate was successfully patterned with Au nanoslits. Figure 2(a) shows a picture of a quarter of the sample substrate before Au film deposition. After Au layer deposition, the substrate was diced to see the cross section of the nanoslits. Figures 2(b) and (c) show images of the sample after Au layer deposition, characterized by AFM and high-resolution SEM (HR-SEM). It is clearly seen that the regular high-density nanoslits have been precisely fabricated. In order to characterize the distance between the nanoslits, a top view approach was applied. A nanogap of about 10 nm is shown in figures 2(d) and (e), with its histogram in figure 2(f) representing the gap distance variation. It can be envisioned that if atomic layer deposition technology could be employed, the surface smoothness would be further improved and the resolution of the nanoslits would be further decreased to the sub-10 nm level.

The metal nanoslit arrays are well suited for plasmonics applications, which use metal nanostructures that couple far-field electromagnetic radiation into electromagnetic surface modes [17]. The confined surface plasmon modes result in an enhanced magnitude of the electromagnetic field at the interface. When two metal nanoslits are in close proximity, the enhanced electromagnetic fields around each nanoslit coherently interfere, resulting in a coupled-plasmon electromagnetic field across the nanogap. Since the gap distance of the nanoslits is controlled by the thickness of the deposited Au layer, a series of Au film thicknesses was prepared by sputtering deposition. An optical absorption measurement was first performed to find the LSPR position. Figure 3(a) shows the spectra on the nanoslit substrates using the reflection mode. For all measurements a flat Au surface is used as a reflectance reference. The reflectance decreases to a minimum value at a certain wavelength corresponding to the LSPR coupling wavelength. It shows clearly that the broad reflection peak (505–509 nm) is slightly red-shifted when the Au layer thickness increases from 67 to 136 nm. This peak becomes flat when the Au thickness is further increased. When the Au film is 179 nm thick, nanogaps of around 10 nm are formed (figure 2(c)) and a second absorption peak (629–634 nm) is obtained (the red line in figure 3(a)). This peak is very sensitive to the change in film thickness, and it

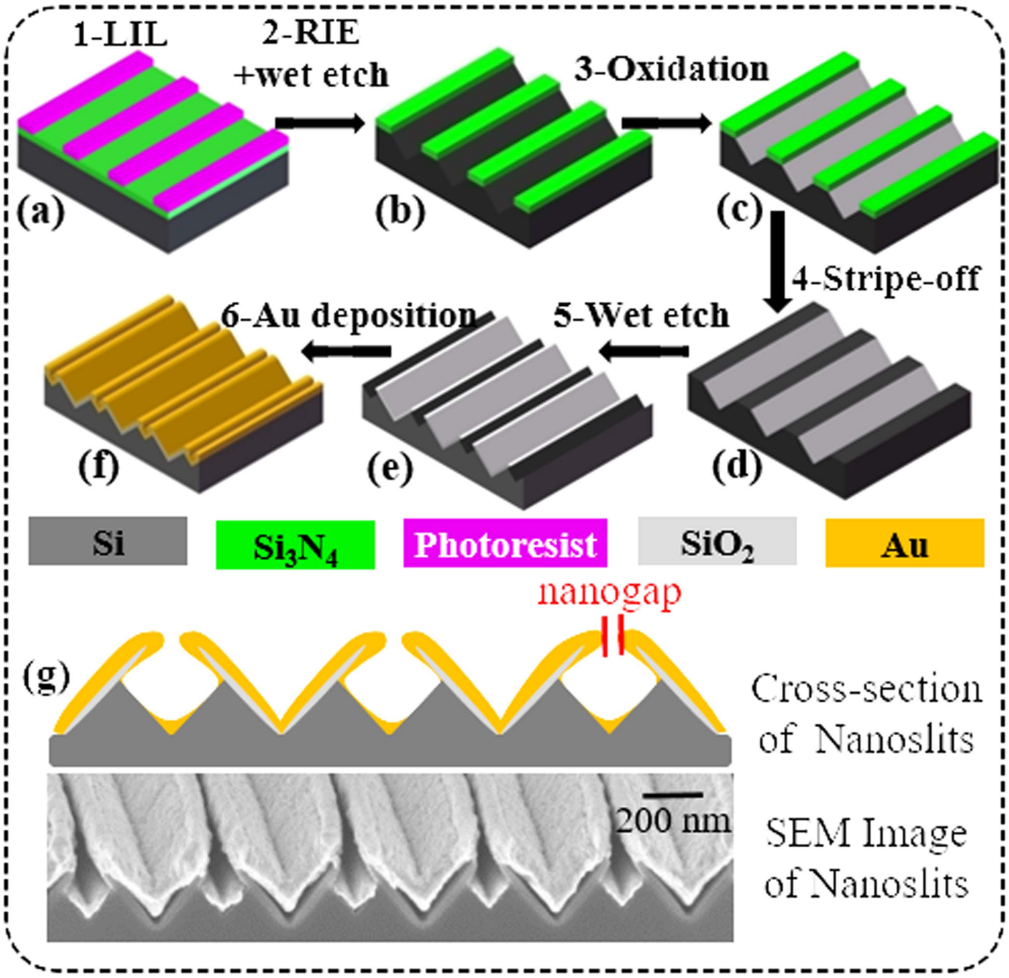

Figure 1. Schematic diagram of the steps of the nanoslit fabrication process using LIL, edge lithography and film deposition: (a) patterning the surface with PMMA, (b) anisotropic wet-etching of silicon to create the 'V'-shaped grooves, (c) oxidizing the exposed Si surface to silicon oxide, (d) removing SiN on the top of the 'V'-shaped grooves, (e) anisotropic wet-etching of the exposed Si on the top to form nanoslits, (f) thin film deposition to create and control the gap distance of metal nanoslits, and (g) the expected cross-sectional view of the fabricated sample (top) and a SEM image of a fabricated sample (bottom).

disappears after deposition of a 19 nm Au layer (giving a total thickness of 198 nm) at which the nanogaps are fulfilled with sputtered Au grains and flattened. Further increasing the Au film thickness to 208 nm shows no difference from the 198 nm Au film sample. This demonstrates a strong dependence of the reflection spectra on the near-field couple-resonance mode in the nanogaps.

The LSPR enhances the electromagnetic field near the nanoslit surface, which provides the basis for plasmonic sensing and SERS [21–26]. Low reflectance at resonance means that a high ratio of the incident light is absorbed and converted to plasmonic excitation, which is largely responsible for the SERS intensity.

Since the nanoslit-induced 'coupling effect' of LSPR will dramatically enhance the Raman scattering signal, Raman scattering measurements were carried out to verify this phenomenon. The Au nanoslit arrays are used as SERS substrates by covering the nanoslit array surface with a monolayer of 4-MBT molecules, which provides an estimation of the uniformity of the spatially averaged enhancement factor from a small number of molecules. 4-MBT is a commonly used as a SERS probe molecule since it has a small number of well-characterized and strong Raman active modes [22]. Two major characterization peaks of the 4-MBT molecules were observed at 1077 cm^{-1} and 1588 cm^{-1}, as shown in figure 3(b). These two peaks are the common SERS peaks of 4-MBT molecules on Au SERS substrates [23]. The 1077 cm^{-1} peak represents a combination of the phenyl ring-breathing mode, C–H in-plane bending and C–S stretching. The other peak at 1588 cm^{-1} can be assigned to phenyl stretching motion (8a vibrational mode) [24].

The nanoslit gap distance is a key factor in generating the 'coupling effect' of LSPR, which determines the Raman signal enhancement. After measuring the Raman signal, we selected the 1077 cm^{-1} peak to investigate how critical is the effect of gap distance on the Raman signal. As shown in figure 3(b), apparent Raman signal enhancement is observed with increase in the Au film thickness. After a certain Au layer thickness the Raman signal decreases again with increasing Au thickness. This means that the major contribution to the SERS signals arises from the nanogaps rather than from the roughness of the surface. These results confirm

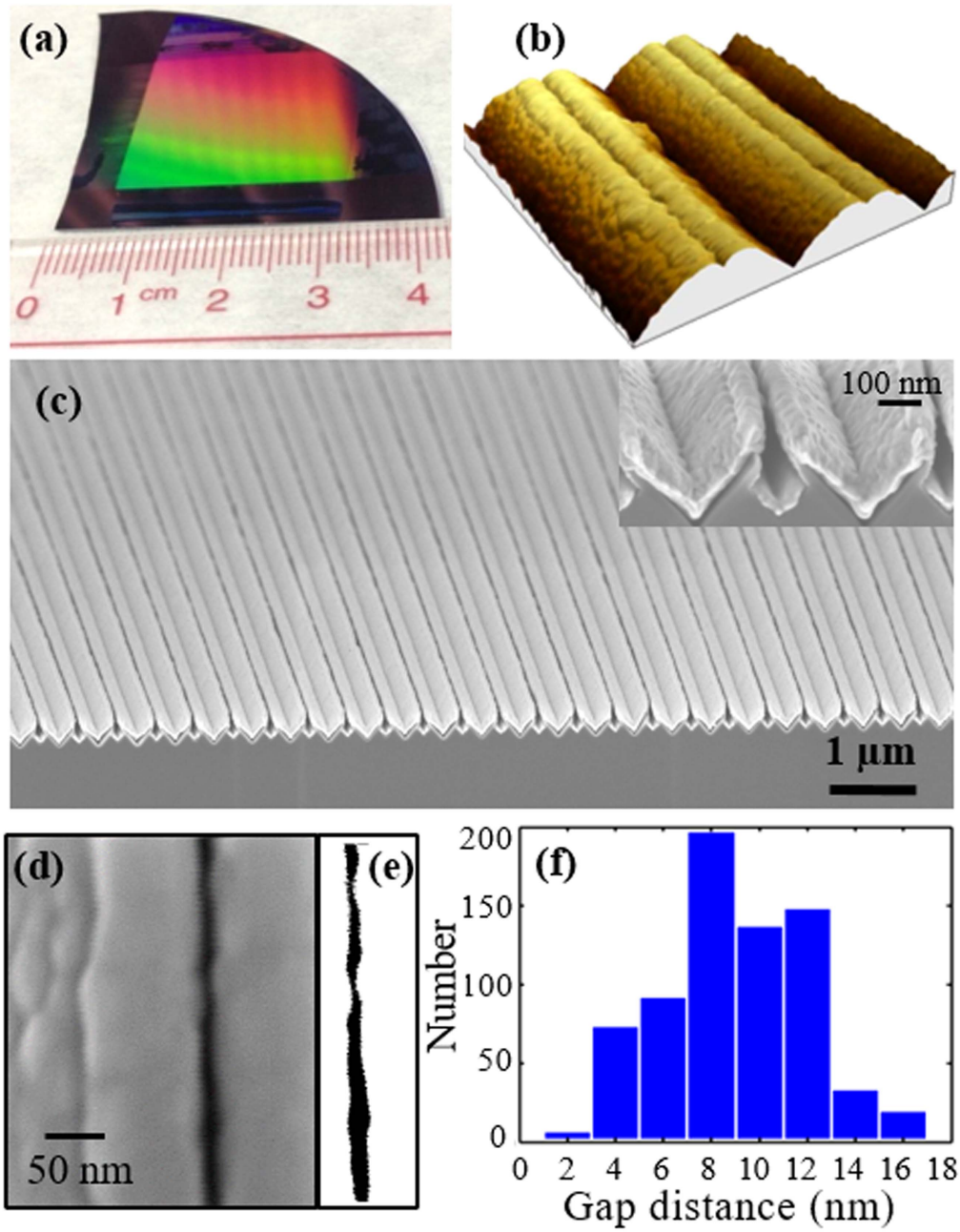

Figure 2. (a) Photograph of a quarter of a 4-inch nanoslit substrate before Au coating. (b) AFM image of a nanoslit sample. (c) HR-SEM images of the large-scale nanoslits with different magnifications. (d) Top view HR-SEM image of a ~10 nm nanoslit. (e) The converted binary image of (d). (f) The histogram of the gap distance of (d). Here, the pitch of the nanoslit array is 500 nm, and Au layer thickness is 179 nm.

that an optimal 'coupling effect' occurs when the thickness of the Au layer is 179 nm, for which the nanogap distance is around 10 nm, as shown in figures 2(d) and (e).

As seen in figure 3(a), there is typically only one working resonance wavelength region for each sample, which means that there is no obvious coupling between cavities with different dimensions in the measured wavelength range of 450–700 nm [11, 12]. The intense SERS signals with 633 nm laser excitation were obtained when an absorption peak of 629–634 nm was obtained at an Au thickness of 179 nm—meaning that the coupled-mode LSPR wavelength in the nanoslit gaps matches the excitation source, thus providing optimal local electromagnetic field enhancement. Both absorption and Raman scattering measurements demonstrate that, with increasing Au film thickness, the LPRS is significantly enhanced, achieving maximum peak intensity at an Au thickness of 179 nm due to the 'coupling effect' of the nanoslits, and then decreases to a plateau (flat surface).

The peak of 1077 cm^{-1} was chosen to estimate the enhancement factor (EF) of the nanoslit 'hot-spots' through the equation $EF = (I_{SERS}/I_{RS})(N_{RS}/N_{SERS})$, where I_{SERS} and I_{RS} are the intensities of the same band of measured Raman signal from the analytical molecules with and without the SERS substrate, respectively, and N_{SERS} and N_{RS} are the

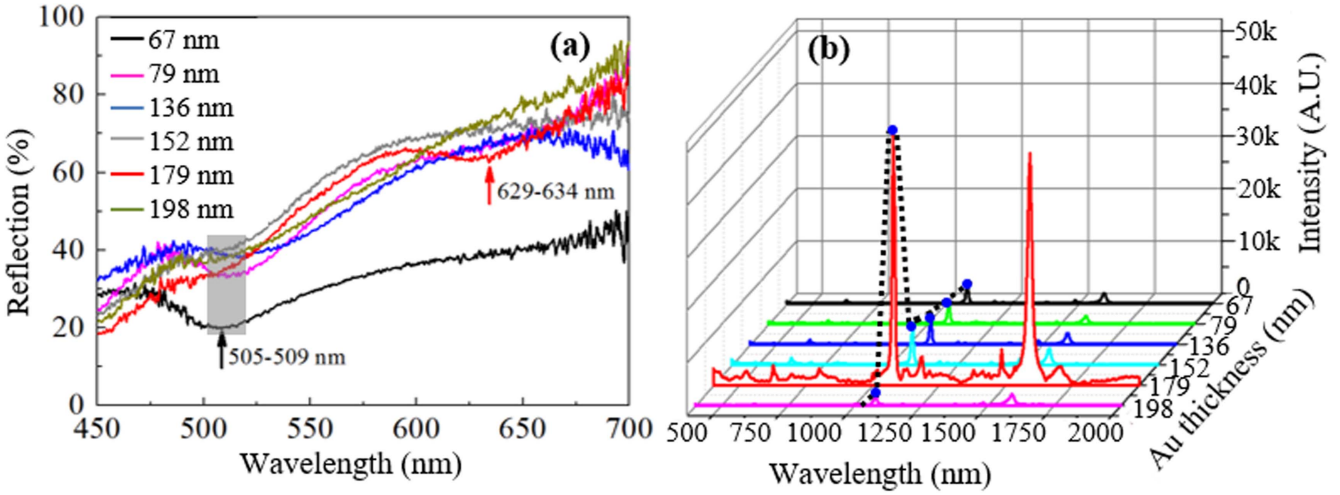

Figure 3. Optical properties of nanoslit array surfaces vary with Au film thickness. (a) Measured absorption spectra of Au nanoslit array surfaces at different Au film thicknesses. (b) SERS spectra of 4-MBT at different Au layer thicknesses. The Au film thicknesses are 67, 79, 136, 152, 179 and 198 nm. 'k' on the *y*-axis stands for 'kilo' in (b).

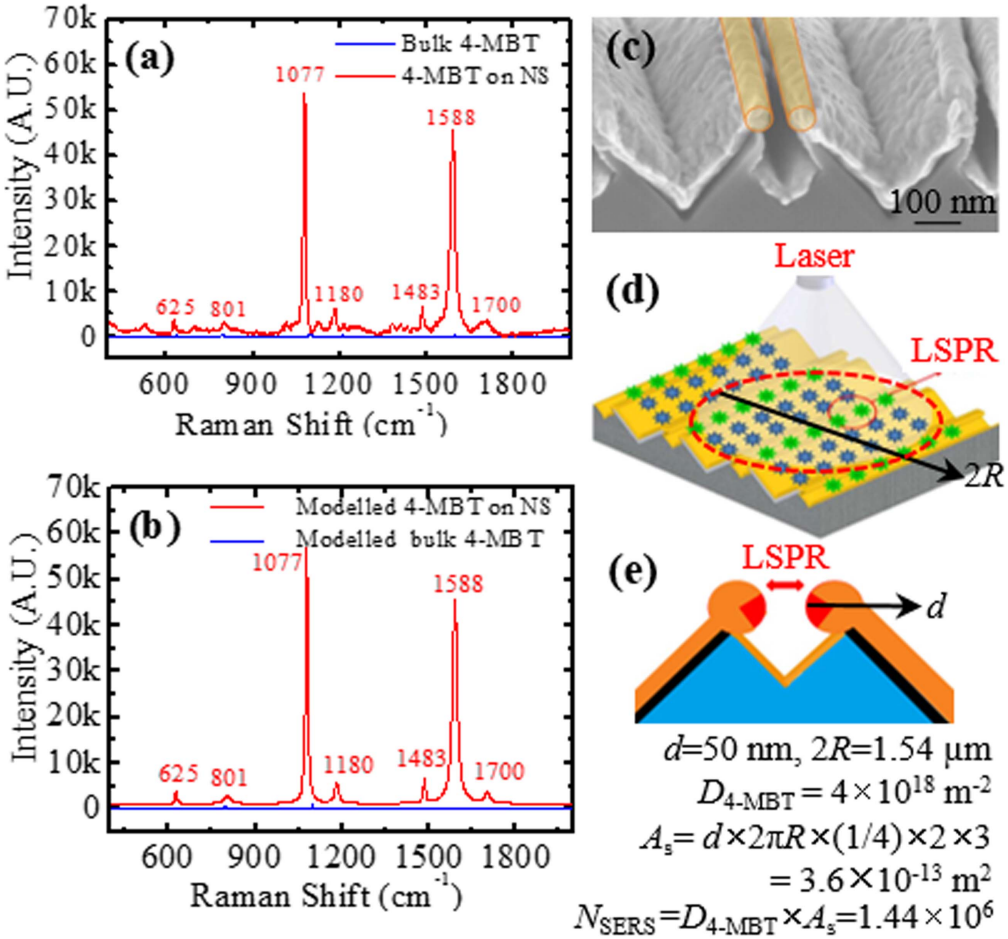

Figure 4. (a) Raman spectra of bulk 4-MBT and 4-MBT on an Au nanoslit substrate. (b) Modelled Raman spectra of bulk 4-MBT and 4-MBT on an Au nanoslit substrate. (c) SEM image of nanoslits (with a cylinder drawing to illustrate our hypothesis). (d) Schematic demonstration of the estimation of the number of probe molecules trapped in the nanoslits (N_{SERS}). (e) The 'hot-spot' region is assumed to comprise a pair of quarter cylinder surface area (red colour). 'k' on the *y*-axis stands for 'kilo' in (a) and (b).

number of the analytical molecules probed in the Raman spectrum with and without the SERS substrate, respectively. In order to accurately calculate the I_{SERS} and I_{RS}, each vibration band of a measured Raman spectrum at each measurement location was modelled with a Lorentzian function and the background signal was modelled with a polynomial function [25]. The integrated intensity of each vibration band was calculated by integrating the area of the fitted Lorentzian function after removing the background signal. The fitting accuracy of the Lorentzian function was comparable to the Voigt functions and used for modelling all measured vibration spectra. Figures 4(a) and (b) show the measured and modelled Raman spectra of bulk 4-MBT and the 4-MBT on an Au nanoslit substrate, showing that the Lorentzian function can well model the Raman spectra. The average integrated intensity of the 1077 cm^{-1} bands of bulk 4-MBT and the 4-MBT on the Au nanoslit substrate was chosen as I_{RS} (74 AU) and I_{SERS} (5.4×10^4 AU), respectively.

N_{RS} was determined based on the Raman spectrum of the solid state 4-MBT and the focal volume of our Raman system (30.88 μm^3). Excited on a pure 4-MBT bulk substrate, the laser excitation volume was assumed to be of a cylindrical shape with a circular diameter equal to the diameter of the focused laser spot and a height equal to the effective probe depth (H_{obj}). H_{obj} was obtained by adjusting the substrate stage out of the focus laser plane at 1 μm increments and recording the Raman peak value at 1077 cm^{-1} at each step. N_{RS} is not counted when the signal intensity is less than half of the maximum value at a characteristic position, yielding $H_{obj} = 16.5\ \mu m$. Therefore, N_{RS} is calculated to be 1.57×10^{11} molecules with a 4-MBT molar volume of 118.3 $cm^3\ mol^{-1}$.

When determining the number of contributing molecules N_{SERS} in the hot-spot region, the equation $N_{SERS} = A_S \times D_{4\text{-}MBT}$ was applied, where A_S is the total contributory nanoslit surface area and $D_{4\text{-}MBT}$ is the surface density of the 4-MBT molecules chemisorbed on the Au(111) surface [27]. 4-MBT molecules are assumed to be absorbed as a monolayer with an average surface density of 4×10^{18} molecules m^{-2} onto the quarter cylinder surface area [24, 27], as shown in figures 4(c)–(e). The diameter of the light spot ($2R$) in our Raman system is 1.54 μm (figure 4(d)) which should include a maximum of three pairs of quarter cylinder diameter (d) (figure 4(e)) based on the SEM images presented in figure 4(c). N_{SERS} was obtained by timing the calculated total surface area of the hot-spot region (A_S) and the surface density of the 4-MBT molecules chemisorbed on the Au (111) surface ($D_{4\text{-}MBT}$), yielding $N_{SERS} = 1.44 \times 10^6$. The EF of the hot-spots was calculated to be 8.0×10^7 based on this approach. N_{SERS} here represents a theoretical maximum number of molecules and is surely an overestimation; therefore, it is likely that the EF value is underestimated rather than overestimated.

4. Conclusion

In summary, we have presented a new strategy for fabrication of large-area and gap-controllable nanoslits, and evaluated and confirmed the LSPR effect of the fabricated nanoslit substrates by SERS measurements. The fabrication strategy is based on a combination of LIL, edge lithography and thin film deposition technologies. LIL is used for quick patterning of the Si surface with around 100 nm resolution and controllable periodicity at a large scale; edge lithography is employed for localized nano-patterning; and Au film deposition is to control the gap distance of the nanoslits, which also brings the advantage of reusability of the SERS substrate. Au nanoslit arrays are presented with the nanogap size down to about 10 nm and a high density of 2.0×10^4 nanoslits per centimetre. The LSPR wavelength on the nanoslit surfaces can be precisely tuned to match the excitation source and provide optimal local electromagnetic field enhancement. The 'coupling effect' of LSPR has been observed at about 629–634 nm wavelength with a maximum peak when Au film thickness is 179 nm, corresponding to the nanoslit gap distance of around 10 nm. A SERS analytical enhancement factor of 8.0×10^7 has been achieved using a 633 nm laser light source to measure 4-MBT molecules chemisorbed on the Au nanoslit substrate. The advantages of this technology include the reproducibility of the fabrication process, the controllability of the gap pitch and distance, the reusability of the template surface by removal and re-deposition of the Au layer, and the possibility of manufacturing nanoslit arrays on a large-area substrate with conventional microfabrication facilities. All these factors would facilitate the cheaper fabrication of large-area nano-featured optical materials and promote their applications and industrialization.

Acknowledgments

We appreciate financial support from Natural Science Foundation of China (61574065 and 21303060), National Key Research and Development Program of China (2016YFB0401502 and 2016YFB0401501), Science and Technology Planning Project of Guangdong Province (2016B090906004), Program for Changjiang Scholars and Innovative Research Team in University (IRT13064), Guangdong Engineering Technology Center of Optofluidics Materials and Devices (2015B090903079), International Cooperation Base of Infrared Reflection Liquid Crystal Polymers and Device (2015B050501010) and Guangdong Innovative Research Team Program (no. 2011D039).

References

[1] Ghosh S K and Pal T 2007 *Chem. Rev.* **107** 4797–862
[2] Brown R J, Wang J, Tantra R, Yardley R E and Milton M J 2006 *Faraday Discuss.* **132** 201–13
Graham D and Goodacre R 2008 *Chem. Soc. Rev.* **37** 883–4
[3] Fan M K, Andrade G F S and Brolo A G 2011 *Anal. Chim. Acta.* **693** 7–25
[4] Huck C, Neubrech F, Vogt J, Toma A, Gerbert D, Katzmann J, Hartling T and Pucci A 2014 *ACS Nano* **8** 4908–14
[5] Nie S M and Emery S R 1997 *Science* **275** 1102–6

[6] Abu Hatab N A, Oran J M and Sepaniak M J 2008 *ACS Nano* **2** 377–85
[7] Baik J M, Lee S J and Moskovits M 2009 *Nano Lett.* **9** 672–6
[8] Ahmed A and Gordon R 2011 *Nano Lett.* **11** 1800–3
[9] Bai S, Zhou W, Lin Y, Zhao Y, Chen T, Hu A and Duley W W 2014 *J. Nanopart. Res.* **16** 1–14
[10] Liu Z, Yang Z B, Peng B, Cao C, Zhang C, You H J, Xiong Q H, Li Z Y and Fang J X 2014 *Adv. Mater.* **26** 2431–9
Xu W G, Xiao J Q, Chen Y F, Chen Y B, Ling X and Zhang J 2013 *Adv. Mater.* **25** 928–33
Dhahi T S, Hashim U and Ahmed N M 2011 *Sci. Adv. Mater.* **3** 233–8
Zhao Y, Berenschot E, Jansen H, Tas N, Huskens J and Elwenspoek M 2009 *Nanotechnology* **20** 315305
[11] Liu Z Q, Liu X S, Huang S, Pan P P, Chen J, Li G Q and Gu G 2015 *ACS Appl. Mater. Interfaces* **7** 4962–8
Liu Z Q, Liu G Q, Huang S, Liu X S, Pan P P, Wang Y and Gu G 2015 *Sensors Actuators B Chem.* **215** 480–8
[12] Liu G Q, Yu M D, Liu Z Q, Liu X S, Huang S, Pan P P, Wang Y, Liu M L and Gu G 2015 *Nanotechnology* **26** 185702
Liu Z Q, Liu G Q, Liu X S, Fu G L and Liu M L 2014 *IEEE Photon. Tech. Lett.* **26** 2111–4
Liu Z Q, Liu G Q, Huang S, Liu X S, Wang Y, Liu M L and Gu G 2015 *IEEE Photon. Tech. Lett.* **27** 1212–5
[13] Im H, Bantz K C, Lindquist N C, Haynes C L and Oh S H 2010 *Nano Lett.* **10** 2231–6
[14] Wu H Y, Choi C J and Cunningham B T 2012 *Small* **8** 2878–85
[15] Kubo W and Fujikawa S 2011 *Nano Lett.* **11** 8–15
[16] Oliveira V, Vilar R, Serra R, Oliveira J C, Polushkin N I and Conde O 2013 *Opt. Laser Technol.* **54** 428–31
[17] Jin M L, van Wolferen H, Wormeester H, van den Berg A and Carlen E T 2012 *Nanoscale* **4** 4712–8
[18] Campbell M, Sharp D N, Harrison M T, Denning R G and Turberfield A J 2000 *Nature* **404** 53–6
[19] Chang T-L, Cheng K-Y, Chou T-H, Su C-C, Yang H-P and Luo S-W 2009 *Microelectron. Eng.* **86** 874–7
[20] Zhao Y, Berenschot E, Jansen H, Tas N, Huskens J and Elwenspoek M 2009 *Microelectron. Eng.* **86** 832–5
[21] Deng X G, Braun G B, Liu S, Sciortino P F, Koefer B, Tombler T and Moskovits M 2010 *Nano Lett.* **10** 1780–6
[22] Endo O, Nakamura M and Amemiya K 2013 *J. Electron Spectrosc. Relat. Phenom.* **187** 72–6
Yin Y, Lu Y, Sun Y and Xia Y 2002 *Nano Lett.* **2** 427–30
[23] Kumar G V P 2012 *J. Nanophotonics* **6** 06450301–20
[24] Li W Y, Camargo P H C, Lu X M and Xia Y N 2009 *Nano Lett.* **9** 485–90
[25] Ngoc L L T, Jin M L, Wiedemair J, van den Berg A and Carlen E T 2013 *ACS Nano* **7** 5223–34
[26] Wei H R, Abtahi S M H and Vikesland P J 2015 *Environ. Sci.: Nano* **2** 120–35
[27] Seo K and Borguet E 2007 *J. Phys. Chem.* C **111** 6335–42